

FULL-WAVE TOMOGRAPHIC AND MOMENT TENSOR INVERSION BASED ON 3D MULTIGRID STRAIN GREEN'S TENSOR DATABASES

Yang Shen

**University of Rhode Island
215 South Ferry Road
Narragansett, RI 02882**

30 April 2014

Final Report

APPROVED FOR PUBLIC RELEASE; DISTRIBUTION IS UNLIMITED.



**AIR FORCE RESEARCH LABORATORY
Space Vehicles Directorate
3550 Aberdeen Ave SE
AIR FORCE MATERIEL COMMAND
KIRTLAND AIR FORCE BASE, NM 87117-5776**

DTIC COPY

NOTICE AND SIGNATURE PAGE

Using Government drawings, specifications, or other data included in this document for any purpose other than Government procurement does not in any way obligate the U.S. Government. The fact that the Government formulated or supplied the drawings, specifications, or other data does not license the holder or any other person or corporation; or convey any rights or permission to manufacture, use, or sell any patented invention that may relate to them.

This report was cleared for public release by the 377 ABW Public Affairs Office and is available to the general public, including foreign nationals. Copies may be obtained from the Defense Technical Information Center (DTIC) (<http://www.dtic.mil>).

AFRL-RV-PS-TR-2014-0124 HAS BEEN REVIEWED AND IS APPROVED FOR PUBLICATION IN ACCORDANCE WITH ASSIGNED DISTRIBUTION STATEMENT.

//SIGNED//

Robert Raistrick
Project Manager, AFRL/RVBYE

//SIGNED//

Glenn M. Vaughan, Colonel, USAF
Chief, Battlespace Environment Division

This report is published in the interest of scientific and technical information exchange, and its publication does not constitute the Government's approval or disapproval of its ideas or findings.

REPORT DOCUMENTATION PAGE				Form Approved OMB No. 0704-0188	
Public reporting burden for this collection of information is estimated to average 1 hour per response, including the time for reviewing instructions, searching existing data sources, gathering and maintaining the data needed, and completing and reviewing this collection of information. Send comments regarding this burden estimate or any other aspect of this collection of information, including suggestions for reducing this burden to Department of Defense, Washington Headquarters Services, Directorate for Information Operations and Reports (0704-0188), 1215 Jefferson Davis Highway, Suite 1204, Arlington, VA 22202-4302. Respondents should be aware that notwithstanding any other provision of law, no person shall be subject to any penalty for failing to comply with a collection of information if it does not display a currently valid OMB control number. PLEASE DO NOT RETURN YOUR FORM TO THE ABOVE ADDRESS.					
1. REPORT DATE (DD-MM-YYYY) 30-04-2014		2. REPORT TYPE Final Report		3. DATES COVERED (From - To) 03 March 2010 to 30 April 2014	
4. TITLE AND SUBTITLE Full-Wave Tomographic and Moment Tensor Inversion Based on 3D Multigrid Strain Green's Tensor Databases				5a. CONTRACT NUMBER FA9453-10-C-0217	
				5b. GRANT NUMBER	
				5c. PROGRAM ELEMENT NUMBER 62601F	
6. AUTHOR(S) Yang Shen				5d. PROJECT NUMBER 1010	
				5e. TASK NUMBER PPM00000915	
				5f. WORK UNIT NUMBER EF004084	
7. PERFORMING ORGANIZATION NAME(S) AND ADDRESS(ES) University of Rhode Island 215 South Ferry Road Narragansett, RI 02882				8. PERFORMING ORGANIZATION REPORT NUMBER	
9. SPONSORING / MONITORING AGENCY NAME(S) AND ADDRESS(ES) Air Force Research Laboratory Space Vehicles Directorate 3550 Aberdeen Avenue SE Kirtland AFB, NM 87117-5776				10. SPONSOR/MONITOR'S ACRONYM(S) AFRL/RVBYE	
				11. SPONSOR/MONITOR'S REPORT NUMBER(S) AFRL-RV-PS-TR-2014-0124	
12. DISTRIBUTION / AVAILABILITY STATEMENT Approved for public release; distribution is unlimited. (377ABW-2014-0664 dtd 11 Aug 2014)					
13. SUPPLEMENTARY NOTES					
14. ABSTRACT A novel framework is developed to construct a 3D Earth model. This new framework results from the marriage of the multigrid method and full-wave tomography: the multigrid method is designed for numerical efficiency, while full-wave tomography is well suited for iterative update of the 3D model. It provides an efficient way to cumulatively and progressively improve the Earth model to as high resolution as observational constraints warrant. Using a new frequency-time data normalization procedure, we show that it is possible to extract up to 600-s period surface waves from ambient noise recorded by broadband seismic stations. These very broadband waves extend surface wave constraints to the crust and entire upper mantle. We collected and processed up to 23 years of continuous seismic data from broadband seismic stations in the eastern hemisphere. A full-wave ambient noise tomographic method is developed and applied to the eastern hemisphere. Three levels of finite-difference computation and inversion are carried out at the hemispherical, continental, and regional scales to progressively construct a hierarchical, multi-resolution P and S velocity model for the eastern hemisphere. The results show a much-improved resolution compared to those of conventional ambient noise tomography and earthquake tomography and provide new constraints on the geological processes in the region. Finally, we determined the moment tensors of earthquakes in southeast Tibet, using strain Green's tensors.					
15. SUBJECT TERMS Full-wave tomography, empirical Green's functions, 3D wave propagation simulation, moment inversion based on 3D strain Green's tensors, nuclear explosion monitoring					
16. SECURITY CLASSIFICATION OF:			17. LIMITATION OF ABSTRACT	18. NUMBER OF PAGES	19a. NAME OF RESPONSIBLE PERSON
a. REPORT	b. ABSTRACT	c. THIS PAGE			Robert Raistrick
Unclassified	Unclassified	Unclassified	Unlimited	32	19b. TELEPHONE NUMBER (include area code)

This page is intentionally left blank.

Table of Contents

1. Summary	1
2. Introduction.....	2
3. Extraction of Very Broadband Empirical Green's Functions	5
4. Full-Wave Tomography.....	7
4.1. Reference Model and Wave Propagation Simulation.....	7
4.2. Phase Delay Measurements	8
4.3 The 3D Sensitivity Kernels	8
4.4. Inversion and the Velocity Model.....	9
5. Model Verification and Validation	11
6. SGT-Based Moment Tensor Inversion	13
6.1 Overview of Moment Tensor Solutions Based on 3D Green's Functions.....	13
6.2 An Example of SGT-Based Moment Tensor Solutions.....	13
7. Results and Conclusions	16
8. Recommendations.....	17
References	18
List of Supplementary Materials.....	22
List of Symbols, Abbreviations, and Acronyms	23

List of Figures and List of Tables

Figures

1. Flow chart of the unified tomography and moment tensor inversions based on 3D finite-difference SGT databases.3
2. Schematic illustration of the multigrid full-wave tomographic framework. Inversion starts from a coarse grid. When the solution converges after several iterations (usually 3 to 4 in our experience), computation is moved to a finer grid in a smaller area. The solution is passed from coarse to fine grids, and vice versa.3
3. A multigrid approach to develop a joint P- and S-velocity model in the eastern hemisphere. The three levels of grids represent the hemispherical-, continental-, and regional-scale models. Red triangles are selected permanent and temporary broadband seismic stations used in inversion. Grey lines are the coast and the 2000-m and 4000-m topographic contours.4
4. Example of EGFs derived from ambient noise (Earth “hum”) with various wave periods (upper left: 50-600 s; upper right: 100-600 s; lower left: 200-600 s; and lower right: 300-600 s). The lines in the accompanying maps show the paths with high signal-to-noise arrivals from the virtual source (station HYB) to other receivers in the eastern hemisphere. The red dots mark a wave propagating at a velocity of 3.9 km/s.6
5. Geometry of typical non-uniform, non-staggered finite-difference grid in a spherical coordinate system.7
6. A snapshot of the seismic response at the surface (vertical ground-motion velocity) to a vertical force at station BJT (Beijing).7
7. Great circle paths of useful Rayleigh wave delays from EGFs at 200-400 s (left), and 75-150 s (right) periods. Triangles mark the locations of seismic stations. Eurasia, northern Africa and Australia are well sampled at all periods used.8
8. Finite-frequency sensitivity of long-period EGFs between BJT (Beijing) and LSA (Lhasa) to V_p (left) and V_s (right) perturbations. The Rayleigh wave period is 150-300 s. The horizontal slice is at ~250 km depth. The sensitivity to V_p is mostly in the upper 100 km. The unit of the sensitivity kernel is s/m^38
9. Comparison of the shear-wave velocity models at 198 km depths from full-wave ambient noise tomography (upper panel) and CUB 2.0 (lower panel, Shapiro and Ritzwoller, 2002). Color indicates the perturbation in percentage relative to the average at the depth. Grey and green lines mark the coast and plate boundaries.9
10. Shear-wave velocity (V_{sv}) at 575 km depth from full-wave ambient noise tomography. Color indicates the perturbation in percentage relative to the average at the depth.10

11. (a) Broadband seismic stations (triangles) used in full-wave ambient noise tomography of the Tibetan plateau. The 3000-m contour outlines the plateau. (b) The shear-wave velocity at depth of ~46 km. The color scale (red to blue) is between 3.59-4.59 km/s. Dashed white lines are the sutures in Tibet, while dashed grey lines are faults. The velocity structures closely follow the geological features. As an indication of resolution, the ductile extrusion of high-grade metamorphic rocks on the southern slope of the Himalaya is imaged as a band of high velocity anomaly.	10
12. Resolution at the hemisphere level. The input (lower panel) and recovered (upper panel) checkerboard velocity perturbations at 163 km depth show good resolution in Eurasia, northern Africa, Australia, and the northern Indian Ocean.....	11
13. Phase delays between the EGFs from the stations in the Tibetan plateau and the synthetic Green's functions for CUB2.0 (black dots) and our new model (red dots) in several period ranges. The error bars represent 1 standard deviation of measurement errors.....	12
14. Solution of the October 27, 2001 (Ms 5.5) Yunnan earthquake. (a-d) Bandpass-filtered observed waveforms (thick gray lines) are compared with the synthetics for the best source solution (red lines). The frequency bands are, from left to right, 0.00833-0.0167, 0.0167-0.0333, 0.0333-0.0667, and 0.0667-0.167 Hz. Dark thick lines are time-shifted observed waveforms used in the final inversion. For the first arrivals (in c and d), the time is reduced to align the arrivals within the time window. The amplitude is normalized by individual trace. (e) Normalized waveform misfit as a function of depth. Crosses mark the grid-search depths. The shaded region indicates the 1- σ confidence limit. (f) Contours of various confidence limits at the depth of the global best solution (8 km for this event). The cross marks the FDSGT location, the square the EHB location, and the diamond the GCMT location. From the innermost contour surrounding the FDSGT solution, the contours are the 68% (1- σ , dark line), 80%, 90%, 95% (2- σ , dark line), and 99% confidence limits. (g) Triangles and cross mark the stations used in the source inversion and the event, respectively. Gray contours follow the sea level, and 2000 and 4000 m elevation.	15
15. Variations of the best moment tensor solution as a function of depth (upper panel) and lateral locations at the global best solution depth (lower panel). The global best solution is shown as the blue-and-white beach ball. The GCMT solution (red-and-white beach ball) is drawn for comparison. The background is shaded topographic relief with known fault traces marked by dashed lines.	16
16. A comparison of the observed waveforms (thick gray lines) and the synthetics for the SGT (solid) and GCMT (dashed) solutions at stations LSA, CHTO and MDJ (triangles). The 200 random realizations of the FDSGT solution are plotted below the observed waveforms to show the range of waveform variation due to uncertainties in the moment tensor solution. The waveforms have been filtered between 0.01667-0.0333 Hz, but not shifted in time. The cross and circle near 26° latitude and 101° longitude are the SGT and GCMT locations, respectively. The channel and time window (after the earthquake origin) are marked above the waveforms.....	16

Tables

1. Model Information	6
----------------------------	---

Acknowledgments

We acknowledge the IRIS DMC for making seismic data available. Seismic Analysis Code (SAC) is used for data processing. Dr. Wei Zhang and Haiying Gao accomplished much of the work discussed in this report. Part of the computation in this study is carried out on a Beowulf PC cluster purchased with a grant from the National Science Foundation (NSF OCE 0727919).

1. SUMMARY

With the rapid increase in seismic data collected around the world, there is an acute need to integrate the available data to construct an accurate and comprehensive Earth model. In this project, we develop a novel framework to construct Earth models by combining the multigrid/multilevel method and full-wave tomography: the multigrid method is designed for numerical efficiency, while full-wave tomography is well suited for iterative update of the 3D model and integration of various seismic data. This new framework provides an efficient way to progressively improve the Earth model to as high resolution as observational constraints warrant. We apply this framework to build a 3D velocity model for the eastern hemisphere that covers Eurasia, Africa, the Middle East, Australia, and the Indian Ocean (latitude 55°S-55°N; longitude 30°W-158°E).

Using a frequency-time data normalization procedure, we show that it is possible to extract up to 300-s period Rayleigh waves from ambient noise recorded by temporary broadband seismic stations and up to 600-s period signals from permanent stations with very broadband sensors. These very broadband waves extend surface wave constraints to all depths of the crust and upper mantle. We collected and processed up to 23 years (1990-2012) of continuous seismic data from all available broadband seismic stations in the eastern hemisphere. Empirical Green's functions (EGFs) extracted from ambient seismic noise are used in full-wave ambient noise tomography developed under this project. Three levels of finite-difference computation and inversion have been carried out at the hemispherical, continental, and regional scales to progressively construct a hierarchical, multi-resolution P and S velocity model. Solutions from the coarse grids are used as initial models for the finer grids and high-resolution models from the finer grids are passed to the coarse grids to be integrated in the next model iteration. The results show much-improved resolution compared to that of conventional ambient noise tomography and earthquake tomography. The new model provides constraints on several geological processes in the region, though detailed geological interpretation is beyond this report. By comparing observed and synthetic waveforms calculated from selected velocity models, we establish a procedure to directly and systematically validate the models. Our results suggest that all future models should undergo rigorous model validation using independent seismic observations.

We extend the 3D Green's function based source moment inversion from local to regional scales and obtain moment-tensor determinations of selected earthquakes in the southeast Tibetan plateau. The solutions are in general agreement with the global centroid moment tensor solutions, though the two source locations may differ by 10s of km. Inspection of waveform fit suggests that regional stations, the 3D reference model and short-period body waves provide tighter constraints on the locations of the earthquakes. The lowest magnitude of the earthquakes in this study is M_w 4.35. As the crustal velocity model improves, short-period (<15 s) surface waves become useful and the SGT-based method may be applied to smaller earthquakes at local and regional scales.

2. INTRODUCTION

There is a general consensus that the use of 3D Earth models improves seismic characterization (Antoun et al., 2008; Covellone and Savage, 2012). Advance in high-performance computation has made it feasible to simulate propagation of increasingly broadband seismic wave in 3D models. Nevertheless it remains impractical to routinely compute forward wave propagation from seismic sources in 3D regional models in real time. One way to overcome this challenge is to take advantage of an important property in seismic wave propagation, the source-receiver reciprocity. The use of the reciprocity property and Green's functions can drastically reduce computational costs when the sources outnumber the stations (e.g., Eisner and Clayton, 2001; Graves and Wald, 2001). More importantly, with 3D Green's functions pre-calculated and saved in a database, they can be extracted quickly from the database after a seismic event and used to determine seismic moments (Zhao et al., 2006; Shen et al., 2014).

The usefulness of 3D Green's functions depends on the accuracy of the corresponding 3D Earth models. By more accurately accounting for the physics of wave propagation in the 3D Earth, the full-wave methods have been proven to be effective in improving model resolution (e.g., Chen et al., 2007b; Tape et al., 2009; Gao and Shen, 2014). Two methods have been developed to date to carry out full-wave tomography. One is the adjoint-wavefield (AW) method, which back-propagates data from receivers to image structure (e.g., Tromp et al., 2005; Liu and Tromp, 2006). The other is the strain Green's tensor (SGT) based, scattering-integral (SI) method, which calculates and stores the sensitivity kernels for each data functional (e.g., Zhao et al., 2005; Chen et al., 2007a,b; Zhang et al., 2007). Both methods are based on simulation of full-wave propagation in 3D models. The main differences are in computation. In general, the AW is CPU intensive, while the SI approach requires a large disk space and fast input/output. One advantage of the SI approach is that the SGT database can be used for source moment inversion in an efficient, global optimization scheme (Shen et al., 2014). For this reason, we focus on the development and application of the SGT-based approach in this project.

Figure 1 outlines the workflow of the unified tomography and source moment inversion based on 3D SGT databases. Station SGTs are constructed from a 3D reference model by finite-difference simulation of the responses to orthogonal unit impulsive point forces acting at the stations. By extracting the SGTs in a small volume surrounding the source reference location, we can invert for source moment tensors and location in a global optimization scheme (Shen et al., 2014). The same SGTs can also be used to calculate the sensitivities of waveforms and their derivatives (phase delays and amplitude anomalies) to source parameters. Forward wave propagation simulation from the source in the 3D reference model provides synthetic waveforms at stations and the wavefield within the volume of the model. Travel time, amplitude, or waveform anomalies are measured from the observed and synthetic waveforms at stations. The forward wavefield (from the source) and the station SGTs are used to calculate the finite-frequency sensitivities to perturbations in V_p , V_s (or bulk and shear moduli), density, and attenuation. Together with the sensitivities to source parameters, the measurements and structural sensitivity kernels are used to invert for the earth structure (e.g., Zhang et al., 2009). The tomographic inversion results and additional constraints (e.g., receiver function solutions, well logs, etc) are added to the 3D reference model. This process can

be repeated to progressively improve the solution. For full-wave tomography using ambient noise data, the source moment inversion is omitted and the synthetic waveforms at stations and sensitivity kernels are all calculated from the SGTs (Shen and Zhang, 2010; Gao and Shen, 2014).

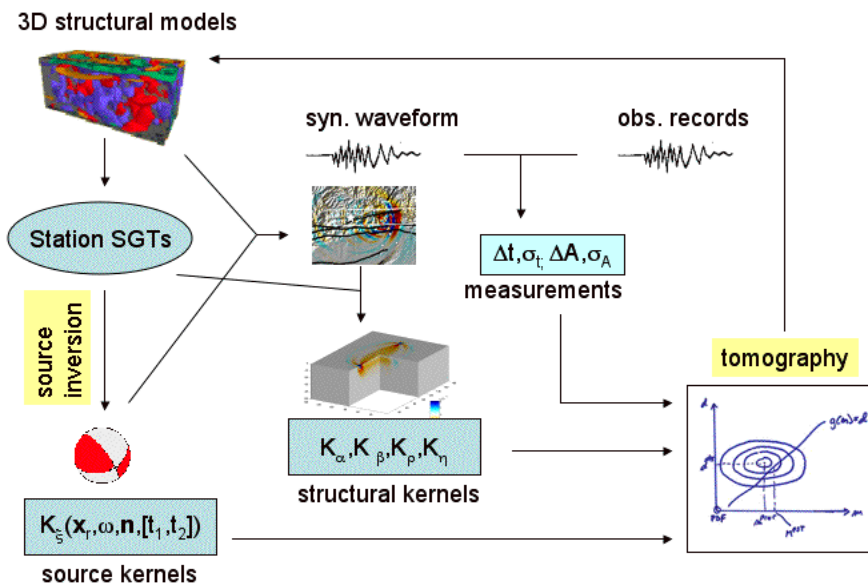


Figure 1. Flow chart of the unified tomography and moment tensor inversions based on 3D finite-difference SGT databases.

One of the main challenges in full-wave tomography is the intense computation associated with simulating wave propagation in 3D models. To reduce computational cost, which generally scales with the number of discrete nodes in numerical methods, we adapt a multigrid/multilevel method (Briggs, 1987) to solve the wave propagation and inversion problem (Figure 2). We use several levels of finite-difference computation with increasingly finer grids at the hemispherical, continental, regional, and local scales to progressively construct a hierarchical, multi-resolution P and S velocity model (Figure 3). Data analysis correspondingly evolves from long-period waves for teleseismic observations to broadband waves for regional and local observations. The solution of a lower (coarser) grid provides the starting model for the next higher (finer) level. The finer-scale solution is then passed to the coarse model for the next model iteration in an iterative,

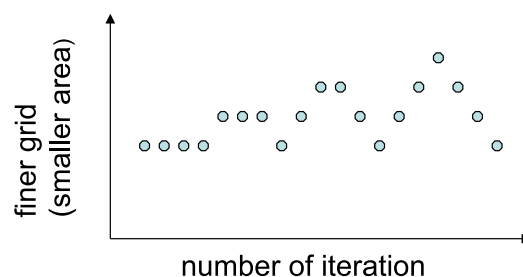


Figure 2. Schematic illustration of the multigrid full-wave tomographic framework. Inversion starts from a coarse grid. When the solution converges after several iterations (usually 3 to 4 in our experience), computation is moved to a finer grid in a smaller area. The solution is passed from coarse to fine grids, and vice versa.

multi-grid scheme (Briggs, 1987). Within this framework, the levels of grids and corresponding multigrid resolution can vary from the global to any survey scales, limited only by the availability of seismic data and computational resources.

The iterative update of the 3D Earth model in full-wave tomography (Figure 1) is well suited for the multigrid method. Together, they provide an efficient way to cumulatively and progressively improve the Earth model. Although each of the lower-level models in this study encompasses one and only one next-level model (Figure 3), several branches of the multigrid model can be developed in parallel (e.g., in Africa, the Middle East, and Australia).

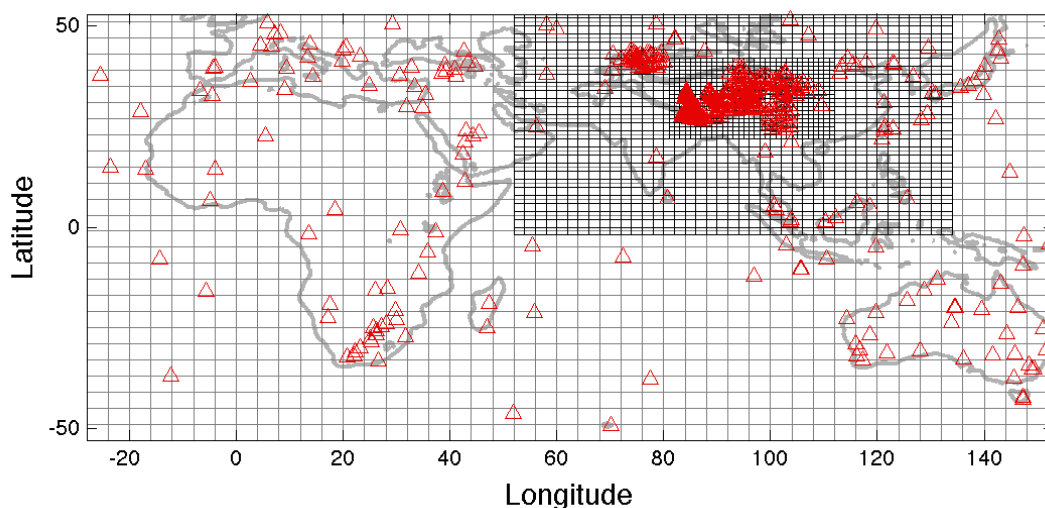


Figure 3. A multigrid approach to develop a joint P- and S-velocity model in the eastern hemisphere. The three levels of grids represent the hemispherical-, continental-, and regional-scale models. Red triangles are selected permanent and temporary broadband seismic stations used in inversion. Grey lines are the coast and the 2000-m and 4000-m topographic contours.

The products of this project include: **(1)** a new non-staggered-grid finite-difference code that simulates wave propagation in a heterogeneous and anisotropic Earth in spherical coordinates (Zhang et al., 2012), **(2)** a frequency-time normalization method that significantly improves the quality of the empirical Green's functions (EGFs) extracted from ambient seismic noise (Shen et al., 2012) and provides very broadband signals that enable imaging of the entire crust and upper mantle, **(3)** a full-wave ambient noise tomographic model of the eastern hemisphere, **(4)** a procedure to validate velocity models (Gao and Shen, 2012; Gao and Shen, in preparation), and **(5)** SGT-based moment tensor inversion (Shen et al., 2014). In the following, we focus on the new ambient noise data processing method (section 3), full-wave ambient noise tomography in the eastern hemisphere (section 4), model validation (section 5), and SGT-based moment inversion (section 6). Concluding remarks and recommendations are presented in Sections 7 and 8, respectively.

3. EXTRACTION OF VERY BROADBAND EMPIRICAL GREEN'S FUNCTIONS

Advance in seismic imaging comes from two main sources: new data sets and new inverse methods. The extraction of EGFs from ambient seismic records is a good example of new data sets: EGFs provide powerful constraints on the Earth's structure, particularly in aseismic regions, because they do not depend on earthquake sources, have precisely known virtual source locations, and yield useful, shorter period surface waves than from earthquakes. Previous ambient noise tomographic studies use short- to intermediate-period (up to ~50 s) surface waves that provide constraints mainly in the crust and uppermost mantle (e.g., Yao *et al.*, 2006; Lin *et al.*, 2008; Yang *et al.*, 2008). In this project, we develop a new data processing method to extract very broadband Rayleigh waves from ambient seismic records, extending EGF constraints to the entire crust and upper mantle (Shen *et al.*, 2012; Shen *et al.*, 2013).

Theoretical and experimental studies have shown that retrieval of Green's functions is best achieved in a diffuse wavefield, in which amplitudes of normal modes are uncorrelated and have equal power (Weaver & Lobkis 2001) or energies radiated by random sources are at the same level (e.g., Snieder, 2004; Curtis & Holliday 2010). However, original seismic records are highly non-stationary and contain local noise, instrument irregularities, and earthquake arrivals. To compensate for the deviation from equal partitioning of noise sources, Stehly *et al.* (2008) showed that the use of the coda of cross-correlation functions helps remediate the problem of anisotropic distribution of noise sources. For applications with a regular and well-sampled array of stations, multidimensional deconvolution (Wapenaar *et al.*, 2011) and directional balancing (Curtis & Halliday, 2010) provide alternatives to the cross-correlation method. But for many passive seismic interferometry problems, cross correlation of records at station pairs remains a commonly used approach.

Bensen *et al.* (2007) provided an excellent review of the cross-correlation-based methods. The two most representative practices of data normalization are one-bit normalization, in which the time series is normalized by its point-by-point absolute value (e.g., Shapiro *et al.*, 2005), and running-absolute-mean normalization, in which the record is normalized by a running average of its windowed absolute value (Bensen *et al.*, 2007). Although long-period surface waves have been observed with these methods (e.g., Shapiro & Campillo 2004; Bensen *et al.*, 2007; Nishida *et al.*, 2009), ambient noise studies using data from temporary broadband experiments typically have useful Rayleigh waves at periods up to 50 s (e.g., Yao *et al.*, 2006; Yang *et al.*, 2008). Using a frequency-time normalization procedure developed under this project, we show that much broader frequency Rayleigh waves can be extracted (Shen *et al.*, 2012).

We have collected and processed continuous data recorded by broadband seismic stations in the eastern hemisphere between 1990 to 2012 (Shen *et al.*, 2013). Data processing follows a nested approach that corresponds to the multi-levels of the study areas (Figure 3, Table 1). For the hemispherical-scale model, for example, we selected ~290 stations having at least 300 days of continuous records for further analysis. Figure 4 shows an example of EGFs from cross correlation of vertical-vertical components of permanent seismic stations. Our results confirm that clear Rayleigh wave signals can be

extracted from seismic “hum”, or earth’s background free oscillation (Nishida et al., 2009). Furthermore we extend the useful period from 400 s (Nishida et al., 2009) up to 600 s! The remarkably good symmetry of very-long period (>100 s) EGFs for the positive and negative time lags of cross correlation indicates a relative homogeneity of noise sources at low frequencies. For PASSCAL broadband stations with 1-2 years’ records, we can extract useful Rayleigh waves up to 300 s period (Shen et al., 2012).

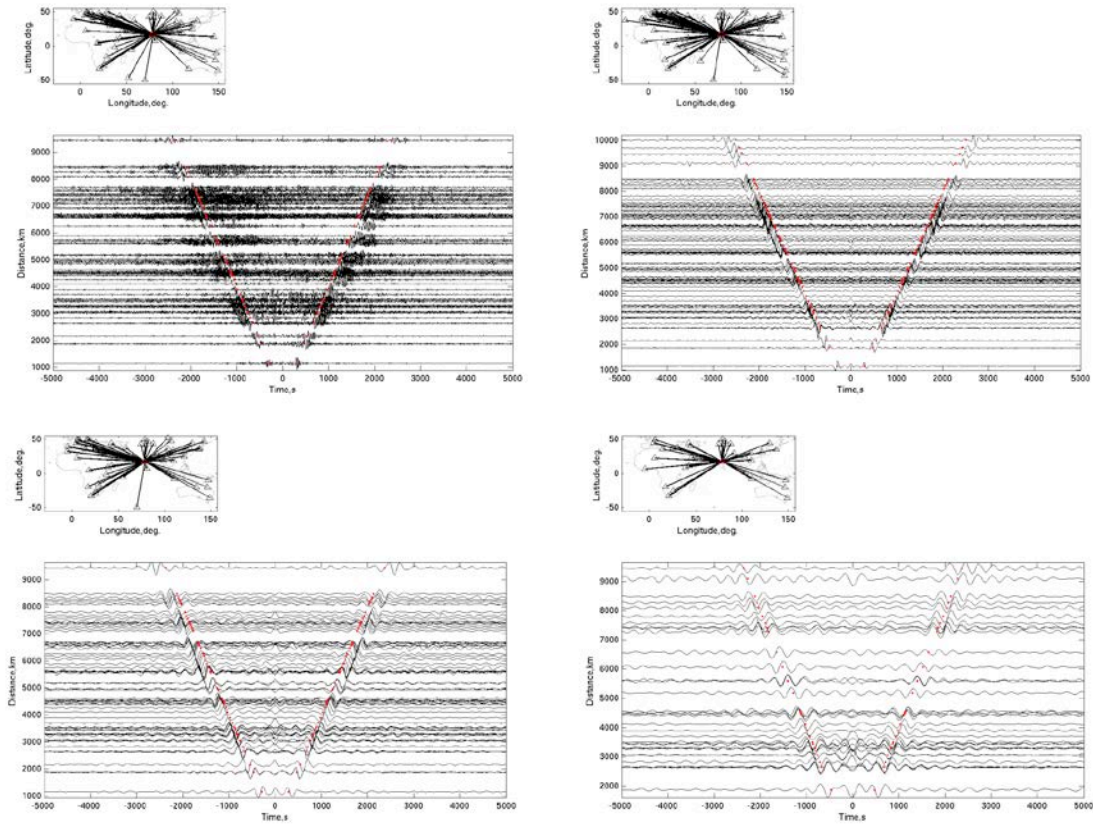


Figure 4. Example of EGFs derived from ambient noise (Earth “hum”) with various wave periods (upper left: 50-600 s; upper right: 100-600 s; lower left: 200-600 s; and lower right: 300-600 s). The lines in the accompanying maps show the paths with high signal-to-noise arrivals from the virtual source (station HYB) to other receivers in the eastern hemisphere. The red dots mark a wave propagating at a velocity of 3.9 km/s.

Table 1. Model Information

Grid/Model Level	number of seismic stations	EGF period range	number of phase measurements	Lateral grid spacing (deg.)	Inversion cell lateral spacing (deg.)
Eastern hemisphere	290	50-600 s	23,000	0.2	2.0
Western China	415	25-300 s	11,000	0.1	1.0
Tibetan plateau	400	12.5-100 s	14,000	0.025	0.5

4. FULL-WAVE TOMOGRAPHY

4.1 Reference Model and Wave Propagation Simulation

The initial 3D reference model for the lowest-level grid is composed of CRUST 2.0 (Bassin et al., 2000) for the crust and AK135 (Kennett et al., 1995) for the mantle. The choice of an average Earth model for the mantle instead of one of the current 3D models (e.g., Ritsema and van Heijst, 2000; Ritzwoller et al., 2002; Antolik et al., 2003) is a tradeoff between finding a good starting model and the need to explore a wide enough model space and verify the final solution.

We use a non-staggered-grid finite-difference code, a code developed under this project, to simulate wave propagation in spherical coordinates (Figure 5, Zhang et al., 2012). The DRP/opt MacCormack scheme, which alternately uses forward and backward finite-difference operators, is implemented in the calculation. The solution is optimized for both dispersion error and dissipation error, and has 4th-order dispersion accuracy. In order to increase the efficiency of the finite-difference algorithm, we use a grid with non-uniform grid spacing to discretize the computational domain. The grid varies continuously with smaller spacing in low velocity layers and with larger spacing otherwise. The computational domain is surrounded by complex-frequency shifted Perfect Matched Layers (PMLs) implemented through auxiliary differential equations (Zhang and Shen, 2010).

For the lowest-level grid, the computational domain covers the eastern hemisphere (latitude 55°S-55°N; longitude 30°W-158°E) with a lateral grid spacing of 0.2°, and a non-uniform grid from the surface to ~2100 km depth (3 km near surface, gradually increasing to ~40 km near the bottom of the model). Tests indicate that the numerical dispersion errors are less than 0.1% for Rayleigh waves with periods greater than 50 s. Figure 6 shows a snapshot of simulated seismic response to a vertical force at station BJI (Beijing). The two higher-level grids (levels 2 and 3) are spaced at 0.1° and 0.025°, respectively,

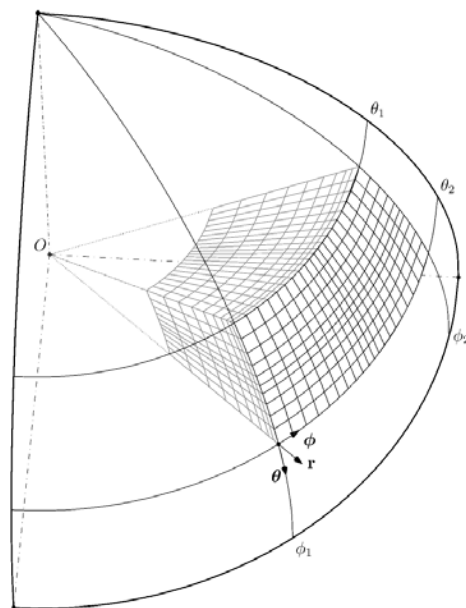


Figure 5. Geometry of typical non-uniform, non-staggered finite-difference grid in a spherical coordinate system.

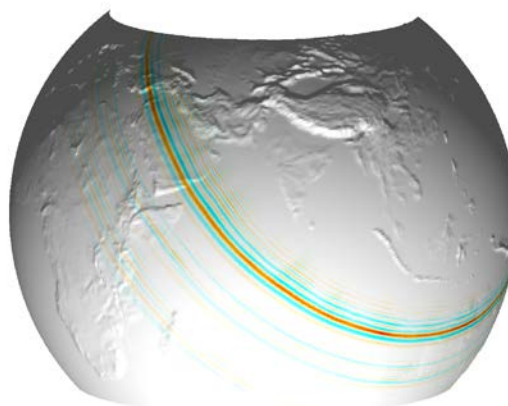


Figure 6. A snapshot of the seismic response at the surface (vertical ground-motion velocity) to a vertical force at station BJT (Beijing).

with correspondingly shorter usable periods of synthetic waveforms (Table 1).

4.2 Phase Delay Measurements

We measure Rayleigh wave phase delays by cross-correlating observed and synthetic Green's functions. For the hemispherical-scale model, the waveforms are band-pass filtered in six period ranges (50-100, 75-150, 100-200, 150-300, 200-400, and 300-600 s). A total of ~23,000 phase delay measurements meet our data selection criteria (waveform correlation coefficient greater than 0.7 and signal-to-noise ratio greater than 5). Most of the propagation paths with useful waves are in the northern hemisphere (Figure 7). Nevertheless the expansion of the initial study area to include stations in the southern hemisphere provides the north-south propagation paths that are essential to obtain good resolution in the north. Table 1 lists the number of stations, frequency range, and number of phase measurements for other grid levels.

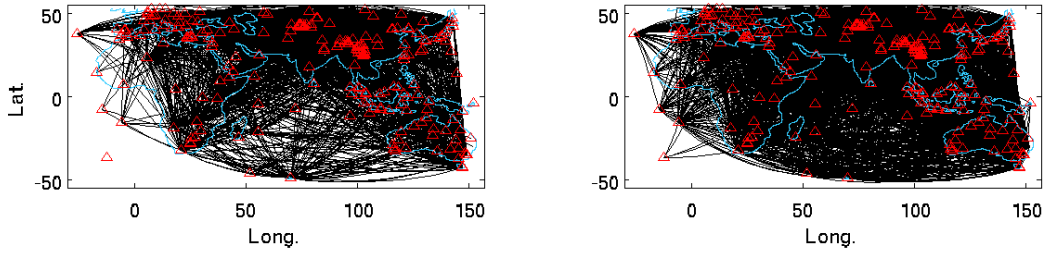


Figure 7. Great circle paths of useful Rayleigh wave delays from EGFs at 200-400 s (left), and 75-150 s (right) periods. Triangles mark the locations of seismic stations. Eurasia, northern Africa and Australia are well sampled at all periods used.

4.3 The 3D Sensitivity Kernels

The cross-correlation of vertical-vertical components at pairs of seismic stations yields predominantly Rayleigh waves in the time window and frequency of our interest. Although commonly neglected in surface wave tomography, P-wave speed affects Rayleigh waves (Figure 8). The sensitivity to P-wave speed is near the surface (the depth of sensitivity increases with period) and at a level comparable to the V_s kernel near the surface. The sensitivity kernels are calculated with the SGT-based, scattering-integral method (Zhao et al., 2005; Chen et al., 2007a; Zhang et al., 2007).

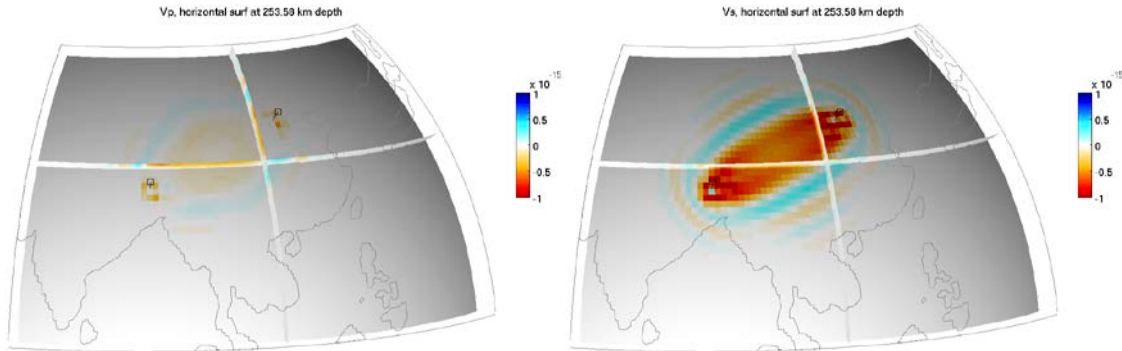


Figure 8. Finite-frequency sensitivity of long-period EGFs between BJT (Beijing) and LSA (Lhasa) to V_p (left) and V_s (right) perturbations. The Rayleigh wave period is 150-300 s. The horizontal slice is at ~250 km depth. The sensitivity to V_p is mostly in the upper 100 km. The unit of the sensitivity kernel is s/m^3 .

4.4 Inversion and the Velocity Model

We represent the Rayleigh wave delays as a joint Vp and Vs inverse problem linearized relative to an iteratively updated 3D model,

$$\delta t = \int [K_\alpha(\mathbf{m}_0, \mathbf{x}) \Delta \mathbf{m}_\alpha + K_\beta(\mathbf{m}_0, \mathbf{x}) \Delta \mathbf{m}_\beta] dV \quad (1)$$

where δt is the travel time delay relative to the synthetics for the 3D model \mathbf{m}_0 , $\Delta \mathbf{m}_\alpha$ and $\Delta \mathbf{m}_\beta$ perturbations to P-wave and S-wave speeds, respectively, K_α and K_β the sensitivity kernels to P-wave and S-wave speeds, respectively. The integration is for the 3D volume of the model. The sensitivity of Rayleigh waves to density is not explicitly expressed in the above equation, but density is updated after each model iteration using a density-Vp relation (Christensen and Mooney, 1995).

The above equation is discretized into inversion cells. For the hemispherical-scale inversion, we use $2.0^\circ \times 2.0^\circ$ blocks as the inversion cells. The thickness of the blocks changes from ~ 14 km near the surface to ~ 80 km at ~ 1600 km depth. The inversion block size is reduced for the higher-level grids to capture sharp velocity changes (Table 1). The size of the inversion cells for level 3 (the Tibetan plateau) is $0.5^\circ \times 0.5^\circ$. The thicknesses of the blocks are proportional to their lateral dimensions.

The inverse problem is solved with LSQR (Paige and Saunders, 1982) with damping and smoothness constraints. The damping and smoothness constraints are gradually reduced until the data misfit is consistent with the estimated data uncertainty (normalized $\chi^2 \sim 1$), as in Montelli et al. (2004). The uncertainty of the phase delays is calculated from the monthly EGF stacks.

Figure 9 is a comparison of the Vs model from this study and that of Shapiro and Ritzwoller (2002), which was derived from group and phase velocities of earthquake surface wave arrivals. Despite the completely different datasets and methods used in the two studies, there are remarkable similarities between the two models. For example, the African cratons and the west Australian craton exhibit

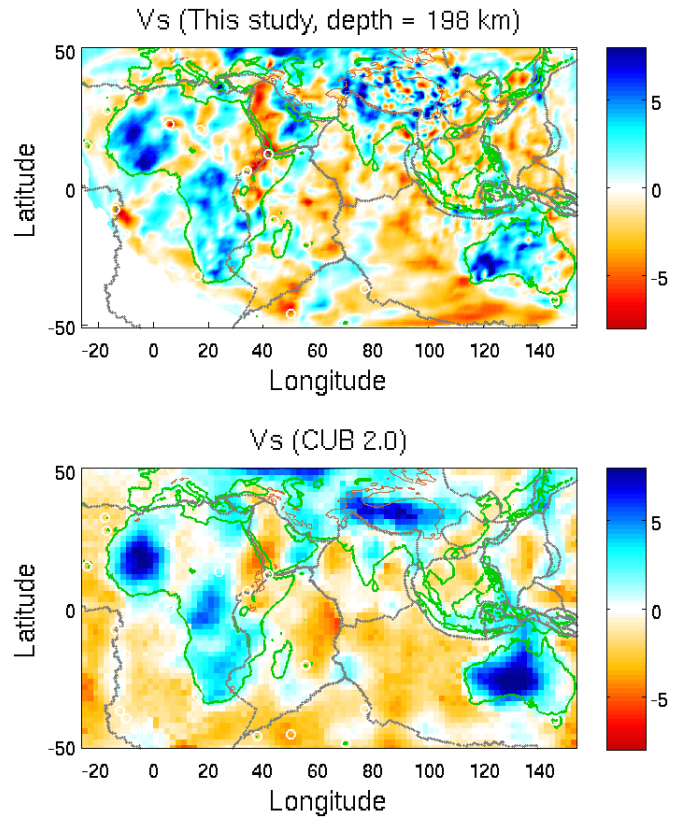


Figure 9. Comparison of the shear-wave velocity models at 198 km depths from full-wave ambient noise tomography (upper panel) and CUB 2.0 (lower panel, Shapiro and Ritzwoller, 2002). Color indicates the perturbation in percentage relative to the average at the depth. Grey and green lines mark the coast and plate boundaries.

high velocity anomalies in both models. The Afar and Eastern Africa Rift are prominent low velocity anomalies in both models. There are also notable differences between the two. The full-wave ambient noise model has resolution in the mantle transition zone (Figure 10), while resolution in CUB2.0 is limited to the upper ~300 km of the mantle due to the limited period range of the earthquake arrivals (< 150 s period). The full-wave ambient noise model also reveals far more detailed structure than in CUB2.0, particularly in west China and the Tibetan plateau (Figures 9 and 11), where full-wave ambient noise tomography with fine grids and dense PASSCAL stations yields much higher resolution. Another notable major difference between the two models is the broad and strong high velocity anomaly beneath the Tibetan plateau in CUB2.0. In our new model, the high velocity anomalies are fragmented beneath the plateau, consistent with body-wave tomography results (Liang et al., 2012), and more prominent in the areas surrounding the plateau, as expected from the presence of the Sichuan Basin (the Yangtze craton) and the Ordos Basin (the North China craton) east of the plateau, the Tarim Basin (the Tarim Archean craton) north of the plateau, and the Indian plate (craton) in the south.

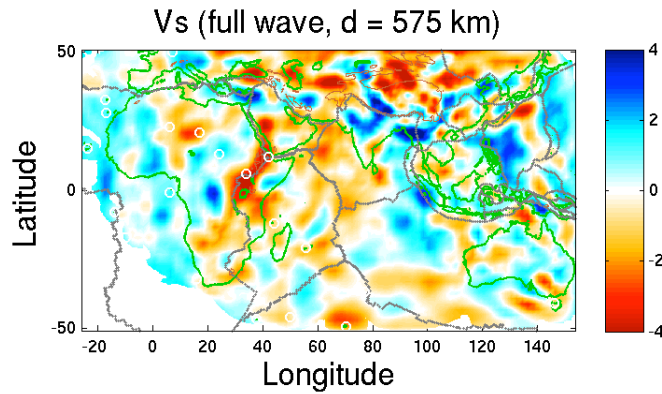


Figure 10. Shear-wave velocity (V_s) at 575 km depth from full-wave ambient noise tomography. Color indicates the perturbation in percentage relative to the average at the depth.

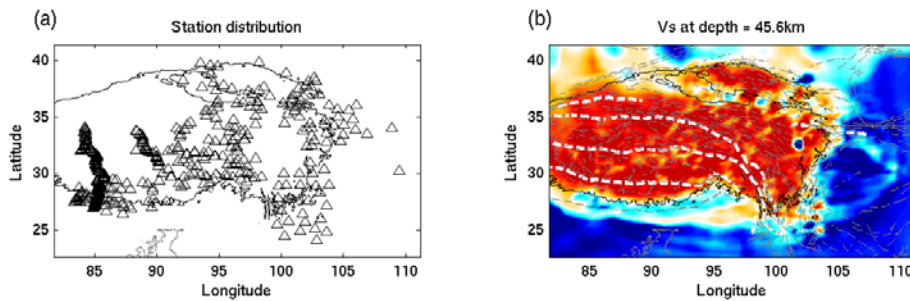


Figure 11. (a) Broadband seismic stations (triangles) used in full-wave ambient noise tomography of the Tibetan plateau. The 3000-m contour outlines the plateau. (b) The shear-wave velocity at depth of ~46 km. The color scale (red to blue) is between 3.59-4.59 km/s. Dashed white lines are the sutures in Tibet, while dashed grey lines are faults. The velocity structures closely follow the geological features. As an indication of resolution, the ductile extrusion of high-grade metamorphic rocks on the southern slope of the Himalaya is imaged as a band of high velocity anomaly.

Synthetic inversion of various input models is a common practice in tomographic resolution analysis. This approach has limitations and can be misleading in the sense that synthetic inversion explores only a limited model subspace (L  v  que et al., 1993). Nevertheless, it is useful if interpretations are restricted to the model subspaces explored. With this caveat in mind, we run 3D checkerboard resolution tests with a maximum of $\pm 5\%$ velocity perturbations for both V_p and V_s at the various grid levels. The synthetic phase delay times are calculated with the sensitivity kernels (Eq. 1). The uncertainties of individual observed phase measurements are estimated from the variations of monthly-stacked EGFs and added to the synthetic phase delays. Figure 12 shows that the results of a checkerboard test at the hemisphere level. The $6^\circ \times 6^\circ$ checkerboard velocity perturbations are well reconstructed in Eurasia, northern Africa, Australia, and the northern Indian Ocean. For $4^\circ \times 4^\circ$ checkerboard velocity perturbations (not shown), western China, the Middle East, the Mediterranean, North Africa, Australia, and the northern Indian Ocean remain well resolved, though smearing becomes obvious at the margins. For the regional scale (level 3), checkerboard tests show that $1^\circ \times 1^\circ$ velocity perturbations are well resolved in eastern and southern Tibet (not shown).

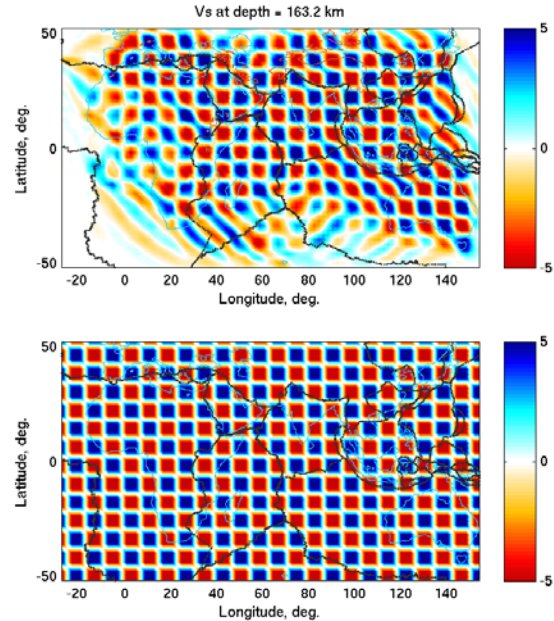


Figure 12. Resolution at the hemisphere level. The input (lower panel) and recovered (upper panel) checkerboard velocity perturbations at 163 km depth show good resolution in Eurasia, northern Africa, Australia, and the northern Indian Ocean.

5. MODEL VERIFICATION AND VALIDATION

There has been an increasing number of published seismic velocity models each year. With models resolved from different methods and datasets comes the need to understand the accuracy and resolution of these models. Becker (2012) quantitatively documented the similarities and differences among several velocity perturbation models resolved from body-wave tomography in the Pacific Northwest. Although the large-scale structures are found to be consistent among these models, the magnitudes of the velocity anomalies vary within a wide range, posing a problem in using the velocity models to infer the structure and dynamics of the mantle in the region.

Although the comparison of various velocity models is helpful, it does not provide an assessment of the validity of the models in predicting seismic observations. A more straightforward and powerful way to validate models is to directly compare the observed and synthetic waveforms (e.g., Song and Helmberger, 2007; Qin et al., 2009; Bozdogan and Trampert, 2010; Gao and Shen, 2012). Using simulation of full wave propagation, Gao

and Shen (2012) systematically tested four surface-wave tomographic models in the Cascades. The results showed that none of the Cascade models is adequately accurate in the sense that the misfits between the observed and predicted seismic waves are much larger than the uncertainty of the observed waveform.

Figure 13 shows a comparison of the phase delays as a function of station separation distance at several frequency bands for CUB2.0 (Shapiro and Ritzwoller, 2002) and our new model of the Tibetan plateau. At long periods (50-100 s), phase delays for CUB2.0 are generally positive and have a positive trend with station separation, indicating that the model is too fast for the real structure beneath the Tibetan plateau. Our new model predicts smaller phase delays that are distributed closely around zero. In order to further understand full-wave tomography, Gao and Shen (manuscript in preparation) carried out a systematic validation of several selected models in north America, where the USArray and unrestricted access to common data sets make the comparison relatively straightforward. The results show that the full-wave tomographic model provides better prediction for both earthquake and EGF arrivals.

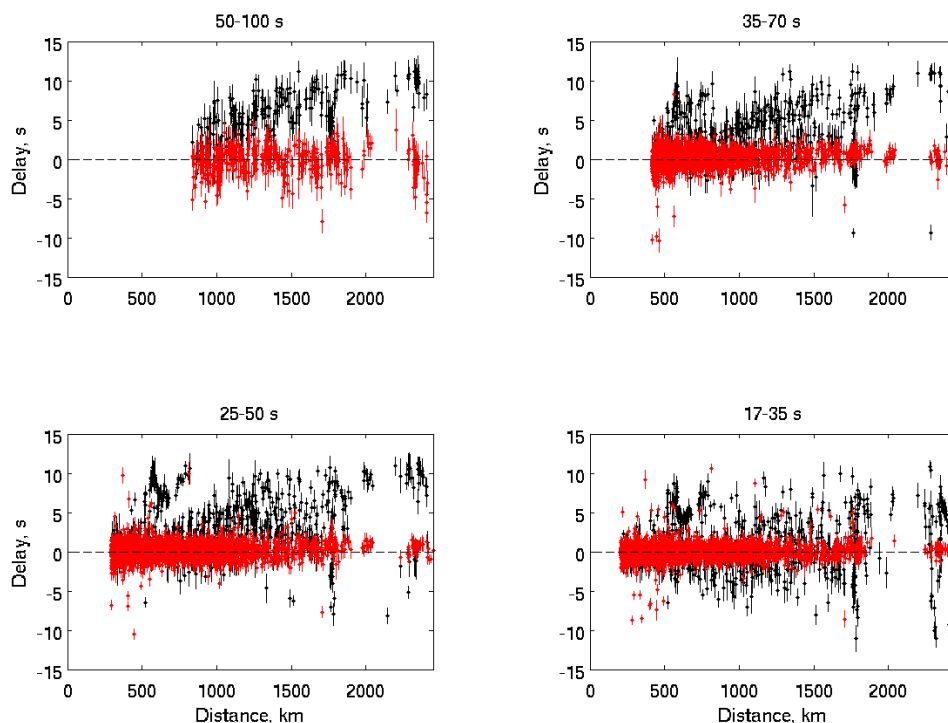


Figure 13. Phase delays between the EGFs from the stations in the Tibetan plateau and the synthetic Green's functions for CUB2.0 (black dots) and our new model (red dots) in several period ranges. The error bars represent 1 standard deviation of measurement errors.

6. SGT-BASED MOMENT TENSOR INVERSION

6.1 Overview of Moment Tensor Solutions Based on 3D Green's Functions

Advances in computation have made the routine use of 3D Green functions in earthquake source inversion an increasingly attractive option. Synthetic waveforms from good 3D reference models account for complex waveform phenomena and reduce phase differences. Liu et al. (2004) determined the source mechanisms of small to moderate earthquakes in southern California using synthetic waveforms calculated with the spectral-element method. Because the derivatives of the source parameters are determined numerically by differentiating synthetics with respect to the source parameters, up to 10 forward simulations are needed for each earthquake (6 moment tensor components, latitude, longitude, depth, and the reference location). When the reference location is far from the true location, the derivatives of the location parameters may not adequately reflect the non-linear variation of waveforms as a function of location.

Taking advantage of source-receiver reciprocity, Zhao et al. (2006) introduced the use of strain Green tensors (SGTs) in source inversion based on 3D reference models. In this approach, the SGTs are calculated with a finite-difference code and saved in a database. The number of forward waveform simulations is three times the number of stations used in source inversion. When the sources outnumber the stations, the Green's tensor or SGT-database approach is more computationally efficient (e.g., Graves & Wald, 2001). More importantly since the SGTs are pre-calculated, the SGT-database approach is better suited for (near-) real-time source inversion. Zhao et al. (2006) adopted a perturbation approach in source inversion and chose to minimize frequency-dependent arrival time and amplitude. In this project, we extend the SGT-database approach from local scales with waveforms calculated in Cartesian coordinates (Zhao et al., 2006) to regional and teleseismic scales with waveforms calculated in spherical coordinates (Zhang et al., 2012), so we are able to use any combination of local and teleseismic waveforms in a source inversion (Shen et al., 2014). Instead of frequency-dependent arrival time and amplitude anomalies, we fit multi-frequency filtered and time-shifted waveforms directly. For a given source location, the waveforms are linear functions of the moment tensor elements, which can be solved as a linear inverse problem. To account for perturbations in earthquake source location, we carry out a grid search in the vicinity of the reference location. This is necessary for earthquakes with location errors of 5 km and more, as is the case for most earthquake catalogs. When the true source location is far from the reference location, the derivative of waveform misfit about the reference location may not be a good approximation to obtain the true location. This in turn affects the waveforms and the moment tensor solution. The grid search is computationally efficient as it involves extracting pre-calculated SGTs in a small volume containing the reference source location from the database. We apply the new method to southeast Tibet in conjunction with a full-wave tomographic imaging effort, as good earthquake source mechanisms are essential for waveform-based tomographic inversions.

6.2 An Example of SGT-Based Moment Tensor Solutions

The October 27, 2001 (Ms 5.5) Yunnan earthquake was recorded by a temporary seismic network (de la Torre et al., 2007) and the permanent stations at regional and

teleseismic distances (Fig. 14g). Body and surface waves at both regional and teleseismic distances in all frequency bands provide useful constraints on the source parameters, though the signals are best in the 30-60 s period range (Fig. 14a-d). Approximately 1/3rd of the frequency-time windows are rejected in the final inversion because of their low signal-to-noise ratios (SNR) or correlation coefficients. The source locations in the EHB and GCMT catalogs differ by ~50 km (Fig. 14f). For moderate and small earthquakes like this one, the difference in location is unlikely the effects of finite spatial rupture, but dominated by location errors (Smith & Ekstrom, 1997). Our new solution is southeast of the EHB location and southwest of the GCMT solution, though the EHB location is within the one- σ uncertainty region defined by waveform misfit and both the EHB and GCMT locations are within the 95% confidence limit. The depth of the preferred solution (8 ± 3 km) is significantly shallower (at the 1- σ uncertainty level) than the GCMT depth (15 km) and the EHB depth (16.7 ± 3.2 km). The waveform fit at the GCMT and EHB depths (15-17 km) is substantially worse than the fit at the best solution (Fig. 14e). Compared to the traveltime-based EHB solution and long-period waveform-based GCMT solution, the depth resolution in this study comes from variations in waveform as a function of the event depth and shorter-period body waves used in this study. If we use the GCMT moment tensor, the waveform misfit is nearly three times larger than that of the best SGT solution (1.64 of GCMT versus 0.52 of SGT).

Figure 15a shows the lowest misfit solution at each grid-search depth. The solutions at very shallow (2 km) and large (> 18 km) depths are noticeably different from the global best solution. In contrast, a ~10 km lateral shift in location does not affect the moment tensor solution significantly (Fig. 15b). This low sensitivity to lateral shift in location is partly due to time shift in waveform fitting to account for errors in the 3D reference model.

A close comparison of the observed waveforms and the synthetics predicted by the GCMT and our SGT solutions reveals that the SGT location yields waveforms that are better matched in time. To illustrate this, we zoom in on the first arrivals at station LSA and CHTO, and the teleseismic S wave at station MDJ (Fig. 16). At station LSA, the GCMT and FDSGT synthetics essentially overlap and both are $\sim 4 \pm 1$ s later than the observed. The delay may result from a ~3% lower-than-real upper mantle P velocity in the reference model. Since a significant portion of the event to LSA path cuts through the Indian mantle indentor, the velocity anomaly seems possible. At station CHTO, the onset of the first arrival from the FDSGT solution matches fairly well with the observed. Changing the source to the GCMT location (and the GCMT moment tensor), we have an onset of the synthetic first arrival that appears ~10 s later than the observed. To fit the arrival, the upper mantle P velocity along the event to CHTO path has to be 8% higher than in the reference model, a value too large to be likely true. At station MDJ, the teleseismic P wave is below the SNR threshold. The synthetic teleseismic S wave from the SGT solution arrives slightly later than that of the GCMT solution and fits the observed better in time.

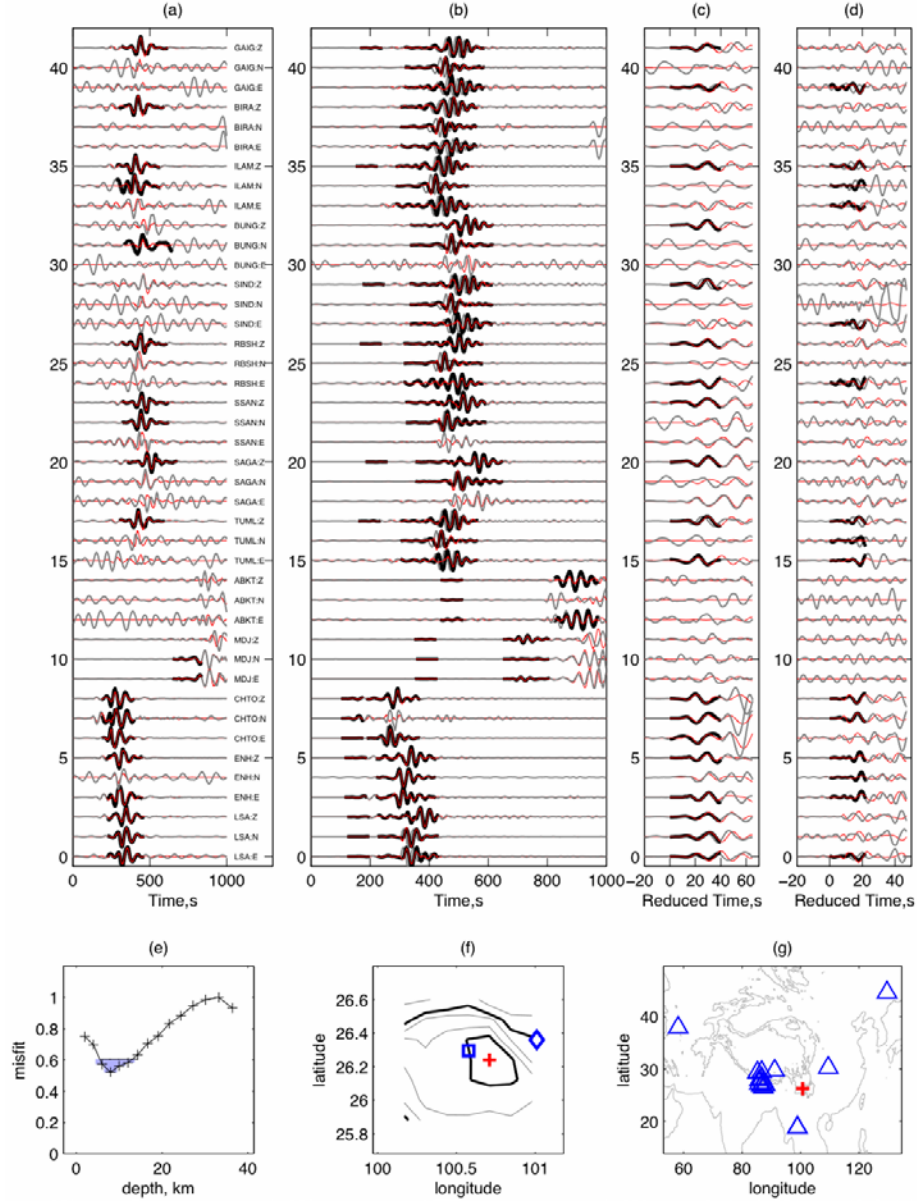


Figure 14. Solution of the October 27, 2001 (Ms 5.5) Yunnan earthquake. (a-d) Bandpass-filtered observed waveforms (thick gray lines) are compared with the synthetics for the best source solution (red lines). The frequency bands are, from left to right, 0.00833-0.0167, 0.0167-0.0333, 0.0333-0.0667, and 0.0667-0.167 Hz. Dark thick lines are time-shifted observed waveforms used in the final inversion. For the first arrivals (in c and d), the time is reduced to align the arrivals within the time window. The amplitude is normalized by individual trace. (e) Normalized waveform misfit as a function of depth. Crosses mark the grid-search depths. The shaded region indicates the 1- σ confidence limit. (f) Contours of various confidence limits at the depth of the global best solution (8 km for this event). The cross marks the FDSGT location, the square the EHB location, and the diamond the GCMT location. From the innermost contour surrounding the FDSGT solution, the contours are the 68% (1- σ , dark line), 80%, 90%, 95% (2- σ , dark line), and 99% confidence limits. (g) Triangles and cross mark the stations used in the source inversion and the event, respectively. Gray contours follow the sea level, and 2000 and 4000 m elevation.

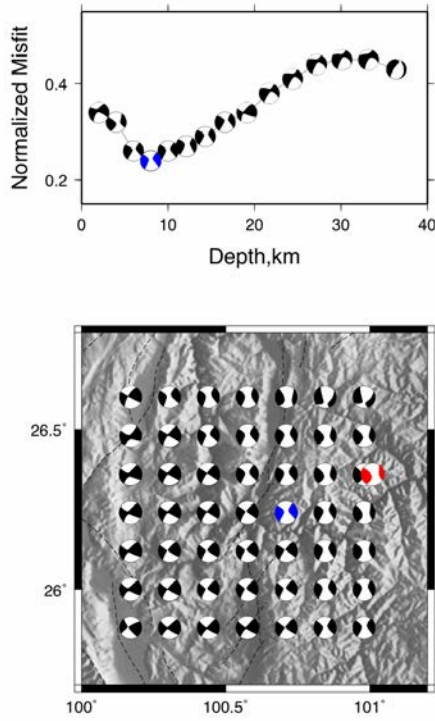


Figure 15. Variations of the best moment tensor solution as a function of depth (upper panel) and lateral locations at the global best solution depth (lower panel). The global best solution is shown as the blue-and-white beach ball. The GCMT solution (red-and-white beach ball) is drawn for comparison. The background is shaded topographic relief with known fault traces marked by dashed lines.

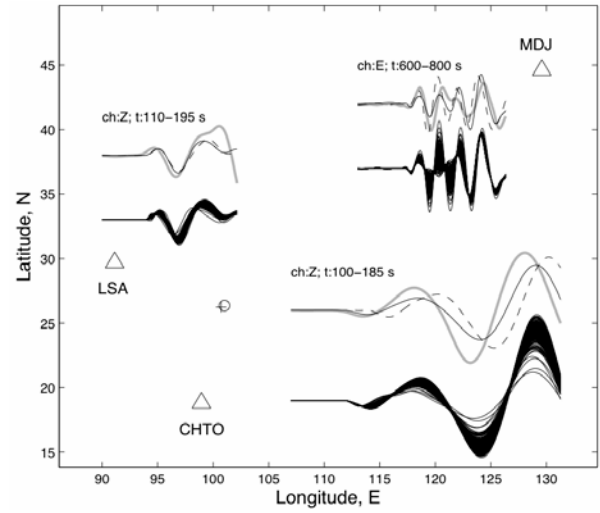


Figure 16. A comparison of the observed waveforms (thick gray lines) and the synthetics for the SGT (solid) and GCMT (dashed) solutions at stations LSA, CHTO and MDJ (triangles). The 200 random realizations of the FDSGT solution are plotted below the observed waveforms to show the range of waveform variation due to uncertainties in the moment tensor solution. The waveforms have been filtered between 0.01667-0.0333 Hz, but not shifted in time. The cross and circle near 26° latitude and 101° longitude are the SGT and GCMT locations, respectively. The channel and time window (after the earthquake origin) are marked above the waveforms.

7. RESULTS AND CONCLUSIONS

We have developed a novel framework in seismic tomography to construct velocity models. This new framework results from the perfect marriage of the multigrid/multilevel method and full-wave tomography and provides an efficient way to cumulatively and progressively improve the Earth model to as high resolution as observational constraints warrant. We apply this framework to build a 3D velocity model for the eastern hemisphere that covers Eurasia, Africa, Mid East, Australia, and the Indian Ocean (latitude 55°S-55°N; longitude 30°W-158°E).

Using a frequency-time data normalization procedure, we show that it is possible to extract up to 300-s period Rayleigh waves from ambient noise recorded by temporary broadband seismic stations and up to 600-s period signals from permanent stations with very broadband sensors (Shen *et al.*, 2012). These very broadband signals help extend

surface wave constraints to all depths of the crust and upper mantle. We collected and processed up to 23 years (1990-2012) of continuous seismic data from broadband seismic stations in the eastern hemisphere (latitude 55°S-55°N; longitude 30°W-158°E).

We have developed a full-wave ambient noise tomographic method (Shen and Zhang, 2010; Gao and Shen, 2014). Three levels of finite-difference computation and inversion have been carried out at the hemispherical, continental, and regional scales to progressively construct a hierarchical, multi-resolution P and S velocity model for the eastern hemisphere. The results show much-improved resolution compared to those of conventional ambient noise tomography and earthquake surface wave tomography (Figures 9 and 13-11). The new model provides constraints on several geological processes in the region, such as the origin of the East African Rift, the extent of underthrusting of the Indian lithosphere beneath Tibet, and recycling of water by subducted slabs. Detailed discussion of the geological implications of the model is beyond the scope of this report.

We extend the SGT-based source moment inversion from local to regional scales and obtain moment-tensor determinations of earthquakes between 2001 and 2004 in the southeast Tibetan plateau (Shen et al., 2014). The SGT inversion takes advantage of the source-receiver reciprocity and is well suited for (near) real time earthquake source studies. The SGT database approach also makes it computationally efficient to determine the best solution in a grid search surrounding the reference location, by minimizing the waveform misfit of time-windowed first arrivals, teleseismic S waves and surface waves recorded at local to teleseismic distances. The new solutions are in general agreement with the global centroid moment tensor solutions, though the two source locations may differ by 10s of km. Inspection of waveform fit in detail suggests that regional stations, the 3D reference model and short-period body waves tend to provide tighter constraints on the locations of the earthquakes. The lowest magnitude of the earthquakes in this study is Mw 4.35. As the crustal velocity model improves, short-period (<15 s) surface waves become useful and the SGT method can be applied to smaller earthquakes at local and regional scales.

8. RECOMMENDATIONS

The multigrid full-wave tomography framework provides a powerful means to progressively add multiple seismic constraints (body and surface waves, receiver functions, reflection/refraction profiles) at various places at any time. To build on this framework, we recommend the following:

- (1) Develop efficient wave simulation methods and codes that take advantage of recent advances in computing technology (e.g., GPUs and many cores);
- (2) Provide a shared-use computing facility at an academic setting (e.g., a university) for researchers in the community to carry out full-wave tomography and exchange/integrate models;
- (3) Provide broad training on the use of the current full-wave tomographic methods;
- (4) Require that all new models are validated against independent seismic observations.
- (5) Collect and maintain a waveform database that contains independently calibrated ground-truth seismic events for model validation

REFERENCES

- Antolik, M., Y. Gu, G. Ekstrom, and A. Dizwonski, 2003, J362D28, a new joint model of compressional and shear velocity in the Earth's mantle, *Geophys. J. Int.* **153**, pp. 443-466.
- Antoun, T., D. Harris, T. Lay, S. C. Myers, M. E. Pasyanos, P. Richards, A.J. Rodgers, W. R. Walter, and J. J. Zucca, 2008, The prospect of using three-dimensional earth models to improve nuclear explosion monitoring and ground motion hazard assessment, Lawrence Livermore National Laboratory Technical Report LLNL-TR-401312.
- Bassin C, G. Laske, and G. Masters, 2000, The current limits of resolution for surface wave tomography in North America, *Eos Trans AGU*, 81, F897.
- Becker, T. W., 2012, On recent seismic tomography for the western United States, *Geochem. Geophys. Geosyst.*, **13**, Q01W10, doi:10.1029/2011GC003977.
- Bensen, G.D., M. H. Ritzwoller, M. P. Barmin, A. L. Levshin, F. Lin, M. P. Moschetti, N. M Shapiro, and Y. Yang, 2007, Processing seismic ambient noise data to obtain reliable broad-band surface wave dispersion measurements, *Geophys. J. Int.* **169**, pp. 1239-1260, doi:10.1111/j.1365-246X.2007.03374.x.
- Bozdag, E. and J. Trampert, 2010, Assessment of tomographic mantle models using spectral element seismograms, *Geophys. J. Int.*, **180**, pp. 1187-1199.
- Briggs, W. L., 1987, *A multigrid Tutoria*, University of Colorado, Denver.
- Chen, P., T. H. Jordan, and L. Zhao, 2007a, Full three-dimensional tomography: a comparison between the scattering-integral and adjoint-wavefield methods, *Geophys. J. Int.*, **170**, pp. 175-181.
- Chen, P., L. Zhao, and T. H. Jordan, 2007b, Full 3D tomography for crustal structure of the Los Angeles Region, *Bull. Seismol. Soc. Am.*, **97** (4), pp. 1094-1120, doi: 10.1785/0120060222.
- Christensen, N. I. and W. Mooney, 1995, Seismic velocity structure and composition of the continental crust: A global view, *J. Geophys. Res.*, **100** (B7), pp. 9761-9788.
- Covellone, B. M. and B. Savage, 2012, A quantitative comparison between 1D and 3D source inversion methodologies: Application to the Middle East, *Bull. Seismol. Soc. Am.*, **102** (5), pp. 2189-2199, doi: 10.1785/0120110278.
- Curtis, A. and D. Halliday, 2010, Directional balancing for seismic and general wavefield interferometry, *Geophys.* **75** (1), SA1-SA14, doi: 10.1190/1.3298736.
- de la Torre, T. L., G. Monsalve, A. F. Sheehan, S. Sapkota, and F. Wu, 2007, Earthquake processes of the Himalayan collision zone in eastern Nepal and the southern Tibetan plateau, *Geophys. J. Int.*, **171**, pp. 718-738.
- Eisner, L. and R. W. Clayton, 2001, A reciprocity method for multiple-source simulations, *Bull. Seismol. Soc. Am.*, **91**, pp. 553-560.
- Gao, H. and Y. Shen, 2012, Validation of shear-wave velocity models of the Pacific Northwest, *Bull. Seismol. Soc. Am.*, **102** (6), pp. 2611-2621, doi:10.1785/0120110336.
- Gao, H. and Y. Shen, 2014, Crust and upper mantle structure of the Cascades with full-wave ambient noise tomography: Seismic evidence for 3D decompressional melting in the back-arc, *Earth Planet. Sci. Lett.*, **390**, pp. 222-233.

- Graves, R. W. and D. J. Wald, 2001, Resolution analysis of finite fault source inversion using one- and three-dimensional Green's functions, 1, Strong motions, *J. Geophys. Res.*, **106**, pp. 8745-8766.
- Kennet, B. L. N., E. R. Engdahl, and R. Buland, 1995, Constraints on seismic velocities in the Earth from traveltimes. *Geophys J Int*, **122**, pp.108-124.
- Lévêque, J. J., L. Rivera, and G. Wittlinger, 1993, On the use of the checkerboard test to assess the resolution of tomographic inversions, *Geophys. J. Int.*, **115**, pp. 313-318.
- Liang, X., E. Sandvol, Y. J. Chen, T. Hearn, J. Ni, S. Klemperer, Y. Shen, and F. Tilmann, 2012, A complex Tibetan upper mantle: A fragmented Indian slab and no south-verging subduction of Eurasian lithosphere, *Earth Planet. Sci. Lett.*, **333-334**, pp. 101-111.
- Lin, F. -C., M. P. Moschetti, and M. H. Ritzwoller, 2008, Surface wave tomography of the western United States from ambient seismic noise: Rayleigh and Love wave phase velocity maps, *Geophys. J. Int.*, doi:10.1111/j.1365-246X.2008.03720.x.
- Liu, Q., J. Polet, D. Komatitsch, and J. Tromp, 2004, Spectral-element moment tensor inversions for earthquakes in southern California, *Bull. Seism. Soc. Am.*, **94**, pp. 1748-1761.
- Liu, Q. and J. Tromp, 2006, Finite-frequency kernels based on adjoint methods, *Bull. Seismol. Soc. Am.* **96**, pp. 2383-2397.
- Montelli, R., G. Nolet, G. Masters, F. A. Dahlen, and S.-H. Hung, 2004, Global P and PP traveltime tomography: rays versus waves, *Geophys. J. Int.*, **158**, pp. 637-654.
- Nishida, K., J. -P. Montagner, and H. Kawakatsu, 2009, Global surface wave tomography using seismic hum, *Science*, **326**, pp. 112.
- Paige, C. C. and M. A. Saunders, 1982, LSQR: An algorithm for sparse linear equations and sparse least squares, *ACM Trans. Math. Software*, 8(1), pp. 43-71.
- Qin, Y., Y. Capdeville, J. -P. Montagner, L. Boschi, and T. W. Becker, 2009, Reliability of mantle tomography models assessed by spectral-element simulation, *Geophys. J. Int.*, **177**, pp. 125-144.
- Ritsema, J. and H. J. van Heijst, 2000, Seismic imaging of structural heterogeneity in Earth's mantle: Evidence for large-scale mantle flow, *Science Progress*, **83**, pp. 243-259.
- Ritzwoller, M. H., N. M. Shapiro, M. P. Barmin, and A. L. Levshin, 2002, Global surface wave diffraction tomography, *J. Geophys. Res.*, **107**, DOI: 10.1029/2002JB001777.
- Shapiro, N. M. and M. Campillo, 2004, Emergence of broadband Rayleigh waves from correlations of the ambient seismic noise, *Geophys. Res. Lett.* **31**, L07614, doi:10.1029/2004GL019491.
- Shapiro, N. M., M. Campillo, L. Stehly, and M. H. Ritzwoller, 2005, High-resolution surface-wave tomography from ambient seismic noise, *Science*, **307**, pp. 1615-1618.
- Shapiro, N. M. and M. H. Ritzwoller, 2002, Monte-Carlo inversion for a global shear velocity model of the crust and upper mantle, *Geophys. J. Int.*, **151**, pp. 88-105.
- Shen, Y., et al., 2013, Construction of a nested, global empirical Green's tensor database, *Seismological Society of America meeting*, Salt Lake City, Utah, April 17-19.
- Shen, Y., Y. Ren, H. Gao, and B. Savage, 2012, An Improved Method to Extract Very Broadband Empirical Green's Functions From Ambient Seismic Noise, *Bull. Seismol. Soc. Am.*, **102** (4), pp. 1872-1877.

- Shen, Y. and W. Zhang, 2010, Full-wave ambient noise tomography of the northern Cascadia, SSA meeting (abstract), *Seismological Research Letters*, **81**, 300.
- Shen, Y., Z. Zhang, and W. Zhang, 2014, Moment inversions of earthquakes in the southeast Tibetan plateau using finite-difference strain Green tensor database, *Geophys. J. Int.*, in revision.
- Smith, G. P. and G. Ekstrom, 1997, Interpretation of earthquake epicenter and CMT centroid locations, in terms of rupture length and direction, *Phys. Earth Planet. Int.*, **102**, pp. 123-132.
- Snieder, R., 2004, Extracting the Green's function from the correlation of coda waves: A derivation based on stationary phase, *Physical Review E* **69**, 046610(8), doi: 10.1103/PhysRevE.69.046610.
- Song, T. -R. A. and D. V. Helmberger, 2007, Validating tomographic model with broadband waveform modelling: an example from the LA RISTRA transect in the southwestern United States, *Geophys. J. Int.*, **171**, pp. 244-258.
- Stehly, L., M. Campillo, B. Froment, and R.L.Weaver, 2008, Reconstructing Green's function by correlation of the coda of the correlation (C3) of ambient seismic noise, *J. Geophys. Res.* **113**, B11306, doi:10.1029/2008JB005693.
- Tape, C., Q. Liu, A. Maggi, and J. Tromp, 2009, Adjoint tomography of the Southern California crust, *Science*, **325**, pp. 988-992.
- Tromp, J., C. Tape, and Q. Liu, 2005, Seismic tomography, adjoint methods, time reversal and banana-doughnut kernels, *Geophys. J. Int.*, **160**, pp. 195-216.
- Wapenaar, K., E. Ruigrok, J. van der Neut, and D. Draganov, 2011, Improved surface-wave retrieval from ambient seismic noise by multi-dimensional deconvolution, *Geophys. Res. Lett.* **38**, L01313, doi:10.1029/2010GL045523.
- Weaver, R. L. and O. I. Lobkis, 2001, Ultrasonics without a source: Thermal fluctuation correlations at Mhz Frequencies, *Physical Review Lett.* **87** (13), 134301(4).
- Yang, Y., M. H. Ritzwoller, F. -C. Lin, M. P. Moschetti, and N. M. Shapiro, 2008, Structure of the crust and uppermost mantle beneath the western United States revealed by ambient noise and earthquake tomography, *J. Geophys. Res.*, **113**, B12310, doi:10.1029/2008JB005833.
- Yao, H., R. D. van der Hilst, and M. V. de Hoop, 2006, Surface-wave array tomography in SE Tibet from ambient noise and two-station analysis – I. Phase velocity maps, *Geophys. J. Int.* **166**, pp. 732-744, doi:10.1111/j.1365-246X.2006.03028.x.
- Zhang, W. and Y. Shen, 2010, Unsplit complex frequency shifted PML implementation using auxiliary differential equation for seismic wave modeling, *Geophys.* **75** (4), pp. 141-154.
- Zhang, W., Y. Shen, and L. Zhao, 2012, 3D seismic wave modeling in spherical coordinate by a non-staggered finite difference method, manuscript to be submitted to *Geophys. J. Int.* **188**, pp. 1359-1381, doi:10.1111/j.1365-246X.2011.05331.x, 2012.
- Zhang, Z., Y. Shen and W. Zhang, 2009, Full-wave finite-frequency tomography of the southeast Tibetan plateau, *American Geophysical Union Fall Meeting* (abstract S31D-08).
- Zhang, Z., Y. Shen, and L. Zhao, 2007, Finite-frequency sensitivity kernels for head waves, *Geophys. J. Int.* **171**, pp. 847-856.

- Zhao, L., T. H. Jordan, K. B. Olsen, and P. Chen, 2005, Fréchet kernels for imaging regional earth structure based on three-dimensional reference models, *Bull. Seism. Soc. Am.* **95**, pp. 2066-2080.
- Zhao, L., P. Chen, and T. H. Jordan, 2006, Strain Green tensor, reciprocity, and their applications to seismic source and structure studies, *Bull. Seism. Soc. Am.* **96**, pp. 1753-1763, doi:10.1785/0120050253.

LIST OF SUPPLEMENTARY MATERIALS

(Publications and Manuscripts Supported or Partially Supported by the Project)

Wave Simulation Method

Zhang, W., Y. Shen, L. Zhao (2012). Three-dimensional anisotropic seismic wave modeling in spherical coordinate by a collocated-grid finite difference method, *Geophys. J. Inter.*, 188, 1359-1381, doi:10.1111/j.1365-246X.2011.05331.x.

Data Processing Method

Shen, Y., Y. Ren, H. Gao, and B. Savage (2012). An Improved Method to Extract Very Broadband Empirical Green's Functions From Ambient Seismic Noise, *Bull. Seismol. Soc. Am.*, 102 (4), 1872-1877.

Full-Wave Ambient Noise Tomography Method and Applications

Gao, H., and Y. Shen (2014). Upper mantle structure of the Cascades from full-wave ambient noise tomography: Evidence for 3D mantle upwelling the the back-arc, *Earth Planet. Sci. Lett.*, 390, 222-233.

Model Validation Method and Applications

Gao, H., and Y. Shen (2012). Validation of shear-wave velocity models of the Pacific Northwest, *Bull. Seismol. Soc. Am.*, 102 (6), 2611-2621.

Gao, H., and Y. Shen (2014). Validation of recent shear-wave velocity models in the United States with full-wave simulation, manuscript in preparation.

SGT-Based Moment Tensor Inversion

Shen, Y., Z. Zhang, W. Zhang (2014). Moment inversions of earthquakes in the southeast Tibetan plateau using finite-difference strain Green tensor database, *Geophys. J. Int.*, under revision.

List of Symbols, Abbreviations, and Acronyms

AFRL	Air Force Research Laboratory
AFSPC	Air Force Space Command
AFWA	Air Force Weather Agency
AW	Adjoint Wavefield
EGF	Empirical Green's Function
EHB	Engdahl-Hilst-Buland earthquake catalog
FD-SGT	Finite-Difference Strain Green Tensor
GCMT	Global Centroid Moment Tensor
PML	Perfectly Matched Layer
SGT	Strain Green Tensor
SI	Scattering Integral

DISTRIBUTION LIST

DTIC/OCP 8725 John J. Kingman Rd, Suite 0944 Ft Belvoir, VA 22060-6218	1 cy
AFRL/RVIL Kirtland AFB, NM 87117-5776	2 cys
Official Record Copy AFRL/RVBYE/Robert Raistrick	1 cy